Magnetic and viscous dynamics of spheroidal nanoparticles

Durhuus, Frederik L.; Beleggia, Marco; Frandsen, Cathrine

Published in:
Physical Review B

Link to article, DOI:
10.1103/PhysRevB.110.144425

Publication date:
2024

Document Version
Publisher's PDF, also known as Version of record

Editors' Suggestion

Magnetic and viscous dynamics of spheroidal nanoparticles

Frederik L. Durhuus [1], Marco Beleggia [2,3] and Cathrine Frandsen [1,*]

[1]*Department of Physics, Technical University of Denmark, 2800 Kongens Lyngby, Denmark*
[2]*Department of Physics, University of Modena and Reggio Emilia, 41125 Modena, Italy*
[3]*DTU Nanolab, Technical University of Denmark, 2800 Kongens Lyngby, Denmark*

(Received 18 June 2024; accepted 23 September 2024; published 15 October 2024)

The shape of magnetic nanoparticles (MNPs) greatly affects their dynamics and their potential as heating agents, e.g., for magnetic hyperthermia treatment of cancer. To investigate shape effects theoretically, we present a computationally efficient model of a uniformly magnetized, spheroid-shaped MNP, suspended in liquid at finite temperature, where the magnetic dynamics are coupled to mechanical rotation. Using exact solutions for the shape-dependent input parameters we vary the aspect ratio from a flat disk, through a sphere to a thin needle shape. By computing the energy absorption rate under an alternating magnetic field, and decomposing the dissipated energy into a frictional and magnetic loss channel, we determine the main heating mechanism in different parameter regimes. We find a critical aspect ratio for maximizing frictional losses, which yields the largest total absorption for a broad range of intermediate applied fields. Depending on the applied field strength, this may increase the absorption rate by over 200% relative to both spherical and highly elongated particles. For stronger fields (larger than about half the anisotropy field given maximal shape anisotropy), magnetic losses dominate for all shapes and extreme elongation is preferable.

DOI: 10.1103/PhysRevB.110.144425

I. INTRODUCTION

Magnetic nanoparticles (MNPs) have a range of current and potential applications including cancer treatment by magnetic hyperthermia [1–3] or by mechanical actuation [4], as well as magnetic particle imaging [5,6] and drug delivery by MNPs [7]. In addition to biomedical applications, MNPs are under study as heating agents in catalytic reactions [8,9] and for inductive components in power electronics [10].

The MNP shape affects both the Brownian response via viscous drag and the Néel response via shape anisotropy. Hence, the response to external magnetic fields is strongly shape dependent.

On the experimental side, MNPs can be reliably synthesized in a broad range of shapes and sizes [11], including shapes with extreme aspect ratios; ranging from flat disks [12–14] to long rods [15,16]. It has been verified that particle shape significantly impacts heating in an applied magnetic field [17,18], transport and stability properties in living tissue [19–21], as well as efficacy and manner of induced cell death during magnetomechanical cancer treatment [4].

On the theoretical and numerical side, there are a number of studies on the dynamics, interaction [22–24] and heating power [25–28] of MNPs in liquid suspension, however these studies predominantly consider idealized, spherical particles with uniform magnetization. While, uniformly magnetized spheres interact like point dipoles, with neat analytical expressions for forces and torques [29], the magnetostatic interactions of nonspherical particles are complicated and numerically demanding [30,31], especially at short range. Also collisions are vastly more complicated for nonspherical particles, and the system parameters increase in complexity. In particular, viscous friction becomes a tensor quantity [32] and there is a shape contribution to the anisotropy [33].

That said, for a lone, single-domain MNP, we find that the computational complexity for arbitrary shapes is comparable to the spherical case. In particular, for a spheroidal particle, i.e., a sphere that is flattened or extended along one axis, there are exact, analytical solutions for both the shape anisotropy [34] and the friction tensor [35].

In this paper we use a lone, uniformly magnetized spheroid as a model system to investigate the effect of shape on the hysteresis dynamics in an ac field. This also serves as a model of highly disperse or weakly interacting MNP suspensions. By tuning the aspect ratio, we interpolate from flat, disk shapes through spheres to needlelike elongated ellipsoids. To evaluate quantities of interest, we use analytical solutions for special cases and Langevin dynamics simulations for the full dynamics at finite-temperature [36,37].

We note that Gavilán *et al.* [17] likewise studied the impact of particle shape on hysteresis numerically. By discretizing the MNP and using micromagnetics, the researchers simulated the finite temperature response of slightly elongated spheroids fixed in space. Also Gubanov *et al.* [38] simulated suspensions of mechanically fixed spheroids; assuming uniform magnetization but including magnetostatic interactions as described in Ref. [39]. Other studies simulated the mechanical motion of ellipsoidal- [40,41], rod- [42,43], or disk-shaped [44] MNPs in liquid suspension, with Ref. [41] considering a magnetically soft, linearly magnetisable ellipsoid. The main methodological advance in the present study is the combination of magnetic and mechanical dynamics. In addition, we

*Contact author: fraca@fysik.dtu.dk

use a recently developed method for decomposing the absorbed and dissipated energy into different transfer channels [36], to elucidate the mechanisms behind hysteresis heating in different parameter regimes.

While this study is limited to ellipsoids of revolution, comparable shapes, like cylindrical disks and rods, are expected to behave similarly. One caveat is that disk-shaped MNPs are typically designed so the ground-state magnetization is either a vortex or two antiparallel domains [14], to limit aggregation by minimizing remanence magnetization. In general, MNPs are uniformly magnetized below a certain critical size, which determines when the present model is applicable. Upper and lower bounds on the critical size have been derived for spheres [45,46] and elongated (prolate) spheroids [47,48], lower bounds for cylinders of all aspect ratios [49], and an approximate lower bound for very flat (oblate) spheroids [50].

Even if the magnetization is uniform in zero-field conditions, a nonspherical MNP in an external field may briefly transition through nonuniform states during moment-reversals. This could affect energy transfer in the magnetic loss regime, but that is outside the scope of this study.

The paper is structured as follows. In Sec. II we present a Langevin dynamics model for a lone, spheroidal MNP in liquid suspension. In Sec. III we analyze the response to an alternating field under the rigid dipole approximation where the magnetic moment is locked to the mechanical rotation. In Sec. IV we include the Landau-Lifshitz-Gilbert (LLG) equation, so the moment can rotate relative to the particles' atomic lattice. Then in Sec. V we propose and test a procedure for estimating the aspect ratio which maximizes heating power in a given applied field.

II. MODEL

We consider a single-domain MNP, with uniform magnetization M in liquid suspension at viscosity η and temperature T. The particle is subject to a uniform magnetic field of the form

$$\mathbf{B} = B\sin(\omega_0 t)\hat{\mathbf{z}}, \tag{1}$$

which is a sine-field of amplitude B and frequency $\omega_0 = 2\pi f$ polarized along z. We denote the net magnetic moment $\boldsymbol{\mu} = \mu\mathbf{m}$ where $\mu = MV$ is magnitude, V is volume, and $\mathbf{m}$ is a unit vector. See Fig. 1(a) for an illustration.

The particle is shaped as a spheroid also known as an ellipsoid of revolution, i.e., an ellipsoid that is rotation symmetric around one axis. We denote the length of the semiaxes a, b, c, and note that $a = b$ by symmetry [cf. Fig. 1(b)]. The geometry is fully specified by a and c or equivalently by the volume $V = \frac{4\pi}{3}a^2c$ and aspect ratio $p = c/a$.

The MNP moves mechanically as a rigid body with velocity $\mathbf{v}$ and angular velocity $\boldsymbol{\omega}$. That is, it rotates at a rate of ω counterclockwise around the vector $\boldsymbol{\omega}$.

A. Anisotropy

We assume uniaxial anisotropy with the anisotropy axis along the local c axis. That is, there is an energy contribution of the form

$$E_{\text{ani}} = -KV(\mathbf{m}\cdot\mathbf{u})^2, \tag{2}$$

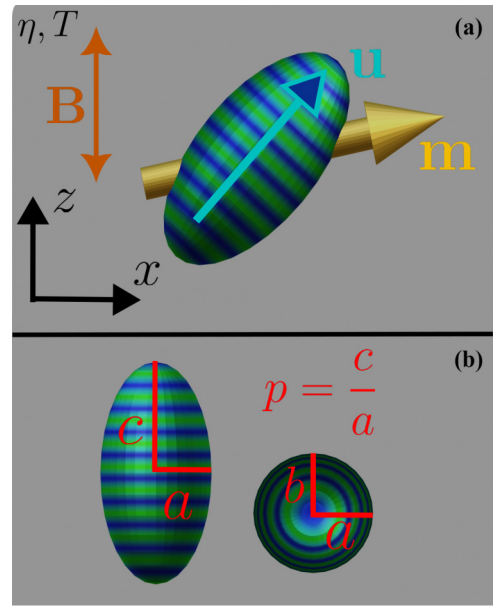

FIG. 1. (a) Illustration of system, i.e., a spheroidal, single-domain magnetic nanoparticle (MNP) suspended in liquid and driven by an external, magnetic field oscillating along z. The normalized moment $\mathbf{m} = \boldsymbol{\mu}/MV$ is indicated, as well as the laboratory xyz-coordinate system. The anisotropy axis is along the rotational symmetry axis and perpendicular to the blue and green circles. (b) Illustration of shape parameters. a, b, c are the principal semiaxes and p is the aspect ratio.

where K is the anisotropy energy density and $\mathbf{u}$ is a unit vector along the anisotropy axis. When $K > 0$ this produces easy-axis anisotropy, where the moment seeks to align with the symmetry axis. Conversely $K < 0$ produces easy-plane anisotropy where the moment seeks the plane perpendicular to $\mathbf{u}$.

In general, K has a shape-, magnetocrystalline-, surface-, and strain contribution [33]. We assume for simplicity that surface and strain contributions are either negligible or shape independent. Then, for a given volume, $K = K_0 + K_{\text{shape}}(p)$ where K_0 is constant.

K_{shape} is derived in Appendix A and plotted in Fig. 2(b). We note that $K_{\text{shape}} = 0$ for a sphere, and is negative for flatter

TABLE I. Simulated parameters.

Symbol	Description	Unit	Values
γ	Gyromagnetic ratio	$\text{s}^{-1}\,\text{T}^{-1}$	1.76×10^{11}
R	Equivalent radius	nm	10
V	Volume	nm^3	4189
p	Aspect ratio	1	0.1...30
T	Temperature	K	0, 300
η	Dynamic viscosity	mPa · s	1
M	Magnetization	kA/m	400
B	Field amplitude	mT	20...300
f	Field frequency	kHz	100
ω_0	$2\pi f$	kHz	200π
K_0	Anisotropy constant	kJ/m^3	20
α	Gilbert damping	1	0.01

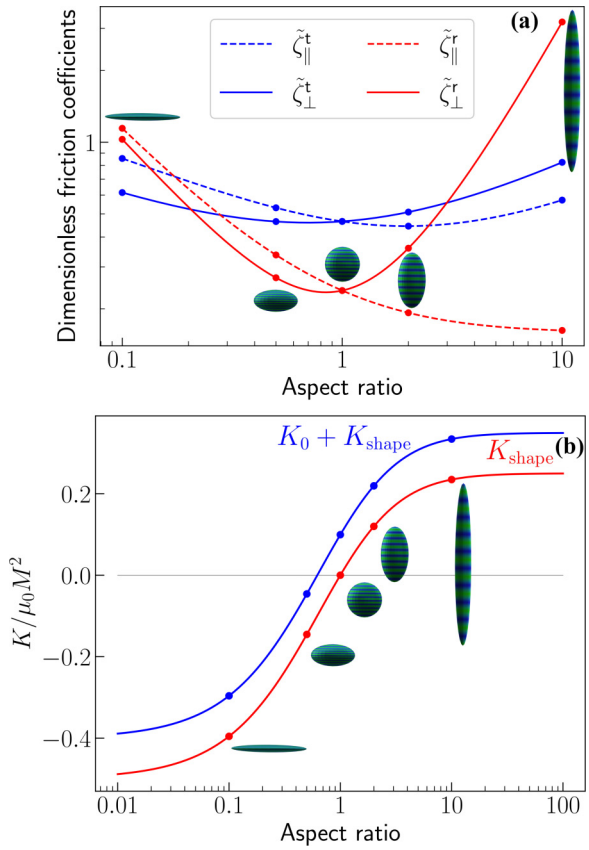

FIG. 2. Parameters that depend on aspect ratio. The shapes simulated in Sec. IV are shown to scale and the corresponding parameter values indicated by dots. (a) Friction coefficients nondimensionalized by $\zeta^{\text{t}}_{\parallel(\perp)} = 8\pi\eta V^{1/3}\tilde{\zeta}^{\text{t}}_{\parallel(\perp)}$ and $\zeta^{\text{r}}_{\parallel(\perp)} = 8\pi\eta V\tilde{\zeta}^{\text{r}}_{\parallel(\perp)}$, where η is the dynamic viscosity. (b) Nondimensionalized anisotropy energy density. The red curve shows the pure shape anisotropy which is material independent. The blue curve is the total anisotropy given the parameters in Table I, which are typical for maghemite.

shapes, but this shape anisotropy may be compensated by a strong out-of-plane magnetocrystalline anisotropy, to ensure a net easy axis.

B. Viscous friction

As the spheroid moves it experiences viscous drag from collisions with the surrounding liquid particles. Because we are considering nanoparticles in liquid, the Reynolds number is small [51] in which case the viscous force and torque for an arbitrary shape are [52]

$$\begin{pmatrix}\mathbf{F}_{\text{visc}}\\ \boldsymbol{\tau}_{\text{visc}}\end{pmatrix} = -\mathrm{Z}\begin{pmatrix}\mathbf{v}\\ \boldsymbol{\omega}\end{pmatrix}, \quad \mathrm{Z} = \begin{pmatrix}\mathrm{Z}_{\text{t}} & \mathrm{Z}_{\text{tr}}\\ \mathrm{Z}_{\text{rt}} & \mathrm{Z}_{\text{r}}\end{pmatrix},$$

where Z is the 6-by-6 friction tensor and $\mathrm{Z}_{\text{t}}, \mathrm{Z}_{\text{r}}, \mathrm{Z}_{\text{tr}}, \mathrm{Z}_{\text{rt}}$ are 3-by-3 tensors.

For the special case of ellipsoids, and other shapes with at least three perpendicular symmetry planes, $\mathrm{Z}_{\text{tr}}, \mathrm{Z}_{\text{rt}} = 0$, i.e., the rotational and translational friction decouple [52,53]. For the spheroid

$$\mathbf{F}_{\text{visc}} = -\mathrm{Z}_{\text{t}}\mathbf{v} \quad \text{and} \quad \boldsymbol{\tau}_{\text{visc}} = -\mathrm{Z}_{\text{r}}\boldsymbol{\omega}, \tag{3}$$

where, in local *abc* coordinates,

$$\mathrm{Z}_{\text{t(r)}} = \begin{pmatrix}\zeta^{\text{t(r)}}_{\perp} & 0 & 0\\ 0 & \zeta^{\text{t(r)}}_{\perp} & 0\\ 0 & 0 & \zeta^{\text{t(r)}}_{\parallel}\end{pmatrix}, \tag{4}$$

where $\zeta^{\text{t}}_{\parallel}$ corresponds to translation along the symmetry axis, $\zeta^{\text{t}}_{\perp}$ to translation in the *ab*-plane, $\zeta^{\text{r}}_{\parallel}$ to rotation around the symmetry axis, and $\zeta^{\text{r}}_{\perp}$ to rotation of the symmetry axis around a vector in the *ab* plane.

There exist a number of schemes for computing Z numerically for arbitrary shapes [54–57], but for the spheroid in particular, exact, analytical solutions are known for all aspect ratios [35,57]. The expressions for all four friction coefficients are given in Appendix B and plotted in Fig. 2(a).

We note that the rotational coefficients have a much stronger shape dependence than the translational. The transverse rotation coefficient $\zeta^{\text{r}}_{\perp}$ is large both for flat and elongated shapes, but the parallel coefficient $\zeta^{\text{r}}_{\parallel}$ is large only for flat shapes. Also, surprisingly enough, the minimum of $\zeta^{\text{r}}_{\perp}$ is not at $p = 1$ (sphere), but at $p = 0.84$ (slightly squashed sphere).

C. Thermal fluctuations

By the fluctuation-dissipation theorem [58], every dissipation mechanism also produces thermal fluctuations. In particular, the thermal motion of the fluid particles leads to random collisions with the spheroid, which produce a stochastic thermal force $\mathbf{F}_{\text{th}}$ and torque $\boldsymbol{\tau}_{\text{th}}$. As is standard, we model these as Gaussian distributed random variables with mean and variance given by [32]

$$\langle F_{\text{th},i}\rangle = \langle \tau_{\text{th},i}\rangle = 0, \tag{5}$$

$$\langle F_{\text{th},i}(t)F_{\text{th},j}(t')\rangle = 2k_B T\mathrm{Z}_{\text{t},ij}\delta(t-t'), \tag{6}$$

$$\langle \tau_{\text{th},i}(t)\tau_{\text{th},j}(t')\rangle = 2k_B T\mathrm{Z}_{\text{r},ij}\delta(t-t'), \tag{7}$$

where k_B is Boltzmann's constant, i, j index vector components, $\langle\rangle$ denotes an ensemble average, and δ is the Dirac δ function. The $\delta(t-t')$ factor signifies zero autocorrelation, i.e., the value at a given point in time is independent of the value at all other times. For a coordinate system where $\mathbf{u}$ is one of the axes, Z is diagonal. It then follows from Eqs. (6) and (7) that each component of $\mathbf{F}_{\text{th}}$, $\boldsymbol{\tau}_{\text{th}}$ is given by an independent Gaussian distribution with variance proportional to one of the friction coefficients.

For the magnetic dynamics, we have the Gilbert damping [59], which is an umbrella term for all the ways the moment, $\boldsymbol{\mu}$, can relax without changing magnitude, e.g., by coupling to lattice vibrations [60]. To the Gilbert damping corresponds the Gaussian distributed, thermal field [61] $\mathbf{B}_{\text{th}}$ given by

$$\langle \mathbf{B}_{\text{th}}\rangle = 0, \quad \langle B_{\text{th},i}(t)B_{\text{th},j}(t')\rangle = \frac{2k_B T\alpha}{\gamma\mu}\delta_{ij}\delta(t-t'), \tag{8}$$

where α is the Gilbert damping constant and γ is the gyromagnetic ratio for an electron.

We note that the derivation of Eq. (8) did not consider mechanical rotation, nor did the derivation of Eqs. (6) and (7) include magnetic dynamics, but we see no physical reason why the magnetomechanical coupling would change either result.

D. Governing equations

The model used in the present paper is a special case of the one developed in Ref. [36], so we refer to Ref. [36] for a detailed derivation.

The general equations of motion for the magnetic dynamics are

$$\dot{\mathbf{m}} = \boldsymbol{\Omega}\times\mathbf{m}, \quad \boldsymbol{\Omega} = \gamma'\mathbf{B}_{\text{eff}} + \alpha\gamma'\mathbf{m}\times\mathbf{B}_{\text{eff}}, \tag{9}$$

where the dot denotes a time derivative, $\boldsymbol{\Omega}$ is an angular velocity for the magnetic moment, and

$$\mathbf{B}_{\text{eff}} = \mathbf{B} + \mathbf{B}_{\text{th}} + \mathbf{B}_{\text{ani}} + \alpha\mathbf{B}_{\text{Bar}}\times\mathbf{m} \tag{10}$$

is the effective B-field.

$$\mathbf{B}_{\text{ani}} = 2\frac{K}{M}(\mathbf{m}\cdot\mathbf{u})\mathbf{u} \tag{11}$$

is the contribution from uniaxial anisotropy and

$$\mathbf{B}_{\text{Bar}} = -\gamma^{-1}\boldsymbol{\omega} \tag{12}$$

is the Barnett field known from the Barnett effect [62], which says that mechanical rotation can induce magnetization changes. Note that only the external field $\mathbf{B}$ extends through space and obeys Maxwells laws.

As shown in Ref. [36], the overdamped limit is extremely well-justified for MNPs in liquid, which means we can neglect mass and moment of inertia entirely. Then, for mechanical rotation,

$$\dot{\mathbf{u}} = \boldsymbol{\omega}\times\mathbf{u}, \quad \mathrm{Z_r}\boldsymbol{\omega} = \gamma^{-1}\mu\dot{\mathbf{m}} + \mu\mathbf{m}\times\mathbf{B} + \boldsymbol{\tau}_{\text{th}}. \tag{13}$$

For translation,

$$\mathrm{Z_t}\dot{\mathbf{r}} = \mathbf{F}_{\text{th}}, \tag{14}$$

where $\mathbf{r}$ is the center-of-mass position. Given the initial values of $\mathbf{m}$, $\mathbf{u}$, and $\mathbf{r}$, the time-evolution of the spheroid is fully described by Eqs. (9), (13), and (14).

Reference [36] also derives expressions for the energy transfer between a collection of MNPs and their environment. Environment refers both to the liquid medium, the sources of external B-fields, and internal degrees of freedom in the MNPs like lattice vibrations and spin wave modes. In the present case, the rate of change of the spheroid energy is

$$\frac{d}{dt}E = P_{\text{hyst}} + P_{\text{mag}} + P_{\text{rot}}, \tag{15}$$

where

$$P_{\text{hyst}} = -\mu\mathbf{m}\cdot\dot{\mathbf{B}}, \tag{16}$$

$$P_{\text{mag}} = -\alpha\mu\gamma^{-1}([\boldsymbol{\Omega}-\boldsymbol{\omega}]\times\mathbf{m})^2 + \mu[(\boldsymbol{\Omega}-\boldsymbol{\omega})\times\mathbf{m}]\cdot\mathbf{B}^{\text{th}}, \tag{17}$$

$$P_{\text{rot}} = -\zeta_{\parallel}^{\text{r}}(\boldsymbol{\omega}\cdot\mathbf{u})^2 - \zeta_{\perp}^{\text{r}}(\boldsymbol{\omega}\times\mathbf{u})^2 + \boldsymbol{\omega}\cdot\boldsymbol{\tau}_{\text{th}}. \tag{18}$$

P_{hyst} is the hysteresis power, that is the power transferred to the spheroid by the external field. The time averaged value $\langle P_{\text{hyst}}\rangle$ may alternatively be estimated by the area of a hysteresis curve. This power is dissipated via magnetic losses from Gilbert damping P_{mag} and viscous losses from rotational friction P_{rot}. The loss powers Eqs. (17) and (18) both have purely dissipative terms proportional to the damping coefficients α, $\zeta_{\perp}^{\text{r}}$, $\zeta_{\parallel}^{\text{r}}$ and terms involving the stochastic vectors $\boldsymbol{\tau}_{\text{th}}$, $\mathbf{B}_{\text{th}}$ which describe two way energy transfer from thermal fluctuations.

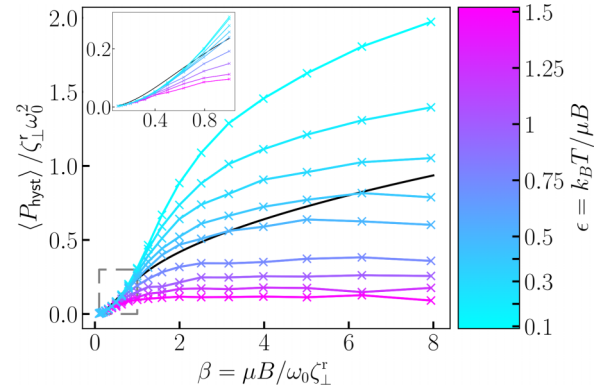

FIG. 3. Simulated absorption rate in the rigid dipole approximation (RDA) as function of the dimensionless parameters $\beta = \mu B/\omega_0\zeta_{\perp}^{\text{r}}$ and $\epsilon = k_B T/\mu B$, which constitutes a completely general solution under the RDA. The black curve shows an integral of the analytical solution over a full period and the crosses are simulated datapoints with lines to guide the eye. For the simulations P_{hyst} has been averaged across a 1000 cycles. The color bar indicates the dimensionless temperature parameter ϵ, with a tick mark for each simulated value. The dashed square corresponds to the inset, which shows the $\beta = 0...1$ results.

Note that power of a positive sign means the MNP is gaining kinetic or potential energy, while negative means energy transfer to the environment.

P_{mag} in particular was used in Refs. [63,64] on systems of mechanically fixed, spherical MNPs, and the full method [(15) to (18)] was tested for spherical MNPs in Ref. [36].

Translational friction can also dissipate energy, but given Eq. (14) the translational power is precisely zero even with thermal fluctuations. This stems from the fact that $\mathbf{B}$ is uniform, so there is complete translational symmetry. Thus, we can safely disregard translation, and the translational friction coefficients $\zeta_{\perp}^{\text{t}}$, $\zeta_{\parallel}^{\text{t}}$ are irrelevant for a lone spheroid.

E. Equivalent sphere

Because of rotational symmetry, we expect $\zeta_{\parallel}^{\text{r}}$ to be relatively unimportant. This is not trivial at finite temperature, as thermal fluctuations cause some rotation around $\mathbf{u}$, however this rotation only couples to the other degrees of freedom via the Barnett field, which is negligibly small for MNPs in liquid suspension [36]. Thus, we can to a very good approximation set $\zeta_{\parallel}^{\text{r}}$ arbitrarily without changing the relevant dynamics.

This means if you construct a sphere with the same transverse friction coefficient $\zeta_{\perp}^{\text{r}}$ and anisotropy constant K as your spheroid, then their dynamics and hysteresis heating are essentially identical. In practice, one could use a nonmagnetic coating layer to increase the drag, specifically you need a hydrodynamic radius of $R_{\text{h}} = (\zeta_{\perp}^{\text{r}}/8\pi\eta)^{1/3}$. For the anisotropy one would have to engineer the other anisotropy energies to balance the shape contribution, or choose an extremely hard magnet where magnetocrystalline anisotropy dominates. We verify the soundness of the equivalent sphere approximation in Sec. IV B 1 and Fig. 4.

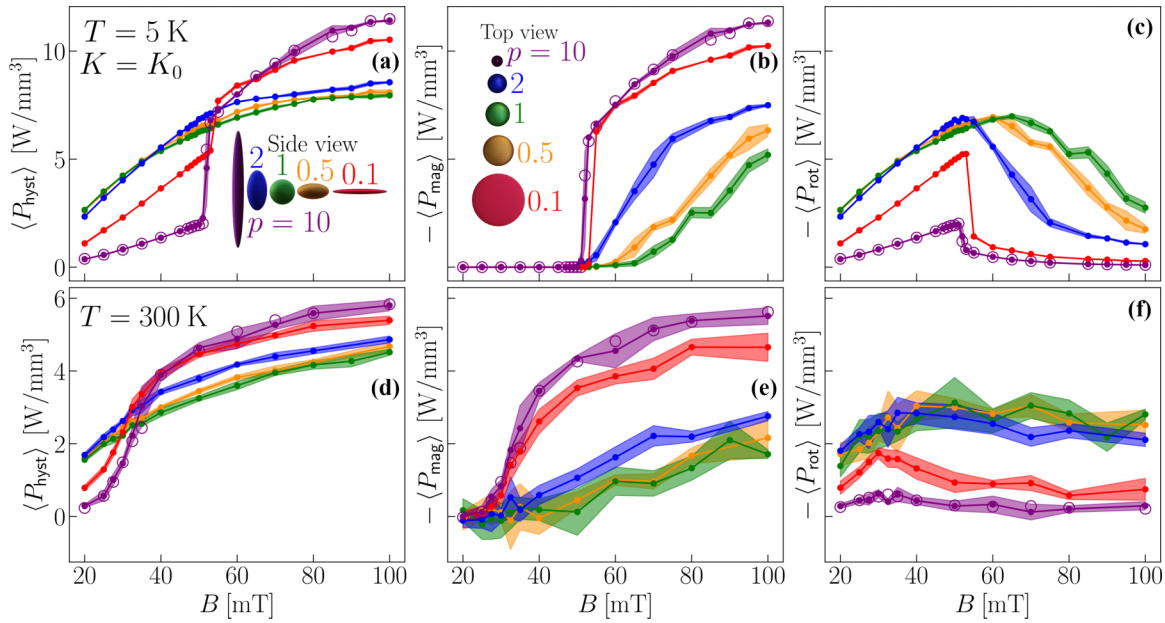

FIG. 4. Time-averaged hysteresis power (a), (d), magnetic losses (b), (e), and viscous, rotational losses (c), (f) at $T = 5$ K (a)–(c) and at $T = 300$ K (d)–(f) as function of applied field strength B for five different spheroids differing only by aspect ratio. Shape anisotropy is neglected (cf. Fig. 5). The shapes are shown to-scale in panel (b) and colored to match the data. The negatives of $\langle P_{\text{mag}}\rangle$ and $\langle P_{\text{rot}}\rangle$ are plotted for ease of comparison with $\langle P_{\text{hyst}}\rangle$, as $\langle P_{\text{hyst}}\rangle + \langle P_{\text{mag}}\rangle + \langle P_{\text{rot}}\rangle = 0$ by energy conservation. Also the same y scale is used in panels (a)–(c) and (d)–(f). Dots indicate datapoints, lines are guides to the eye and circles are simulations of the equivalent sphere. Each datapoint is the average of three simulations (a)–(c) and five in (d)–(f), with colored regions indicating standard deviation. See Table I and Fig. 2 for parameter values.

The notion of the equivalent sphere is especially useful for modeling purposes as one can take existing studies, models and software tools for spheres and apply to lone spheroids simply by changing the input parameters. However, we emphasize that anything which breaks the rotational symmetry also negates the equivalence to a sphere. For example higher order anisotropy terms[33,65] or interactions with other particles.

III. LOCKED MAGNETIC MOMENT

When the anisotropy energy Eq. (2) is positive ($K > 0$) and large compared to the other MNP energy scales, like thermal energy, the magnetic moment will tend to stay fixed along the anisotropy axis without flipping. Then the moment is locked to the particles' mechanical rotation, so we can set $\mathbf{m} = \mathbf{u}$ and ignore the LLG equation altogether. This is known as the rigid dipole approximation [36,66,67] (RDA), though locked moment approximation is arguably more appropriate. Additionally, the $\gamma^{-1}\dot{\boldsymbol{\mu}}$ term in Eq. (13) is negligible in liquid under the RDA [36].

In Appendix C we analyze the model in Sec. II D subject to the RDA. The main takeaway is that with the dimensionless time $\tilde{t} = \omega_0 t$ and frequency $\tilde{\boldsymbol{\omega}} = \boldsymbol{\omega}/\omega_0$ the MNP dynamics are fully described by just two dimensionless parameters:

$$\beta = \frac{\mu B}{\omega_0 \zeta_\perp^{\text{r}}}, \tag{19}$$

$$\epsilon = \frac{k_B T}{\mu B}. \tag{20}$$

ϵ is the thermal energy relative to the Zeeman energy, which describes the degree of thermal fluctuations. β is the ratio of the characteristic frequency for mechanical rotation $\mu B/\zeta_\perp^{\text{r}}$ and the driving frequency ω_0. As we verified by simulations, β measures how far the external field can rotate the particle in a field cycle.

RDA simulations

In the RDA, hysteresis results exclusively from the magnetic moment lacking behind the applied field due to viscous drag, rather than magnetization reversals. In fact $P_{\text{mag}} = 0$ and all the absorbed energy has to eventually be dissipated via viscous losses, hence in steady-state $\langle P_{\text{hyst}}\rangle = -\langle P_{\text{rot}}\rangle$ where $\langle\rangle$ denotes a time-average over a number of full cycles. In Fig. 3 we present a numerical solution for the absorption rate $\langle P_{\text{hyst}}\rangle$ as function of β and ϵ, with a comparison to the zero temperature analytical solution derived in the Supplemental Material [68]. The numerical implementation is a reduced version of the algorithm in Appendix D.

Comparing the $T = 0$ solution (black curve) to the $\epsilon = 0.1$ low-temperature simulation, we see a difference of up to a factor 2. As discussed in the Supplemental Material [68] this stems from an unrealistic time-symmetry present in zero temperature models, so we restrict further analysis to finite temperature dynamics.

From the numerical solutions in Fig. 3 we observe that decreasing T will always increase $\langle P_{\text{hyst}}\rangle$ in the RDA; that is cold particles are more efficient at hysteresis heating. For a cold particle, the motion is completely driven by the applied

field, while for a hot particle thermal fluctuations interfere with the field-particle coupling, thus limiting the energy transfer. Increasing field strength and magnetization will always raise P_{hyst}. At low β, this is because raising μB increases the degree of rotation. At high β and ϵ, the $P_{\text{hyst}}(\beta)$ curve is flat, because the particle fully rotates and thermal noise limits how suddenly it can happen, however increasing μB also reduces ϵ, i.e., quenches the thermal noise.

The effect of ω_0 and $\zeta_\perp^{\text{r}}$ are harder to infer because they enter in both β and the normalized power $\tilde{P}_{\text{hyst}} = \langle P_{\text{hyst}}\rangle/\zeta_\perp^{\text{r}}\omega_0^2$. However, one may prove that $\langle P_{\text{hyst}}\rangle$ is maximized with respect to $\zeta_\perp^{\text{r}}$ (keeping μ, B and ω_0 constant) precisely when $\tilde{P}_{\text{hyst}}$ is linear in β, i.e., at inflection points (see Appendix C 2). From the curvature of the $\epsilon = 0.1$ lightblue curve, we find a critical value of $\beta = 1.3$, though this decreases with temperature. Thus, tuning the friction coefficient so $\beta \sim 1$ (e.g., via particle shape) maximizes energy absorption and dissipation from mechanical rotation. The explanation is that when β is small, lowering the friction enables more rotation, while for $\beta \gg 1$ the applied field rotates the particle a full 360° per cycle, so greater resistance from friction implies more energy dissipation.

IV. FREE MAGNETIC MOMENT

For the full spheroid dynamics described by Eqs. (9), (13), and (14) K becomes a model parameter, yielding the additional dimensionless parameters

$$\kappa = \frac{KV}{\mu B} = \frac{K}{MB}, \tag{21}$$

$$\sigma = \frac{KV}{k_B T}. \tag{22}$$

κ is the ratio of the characteristic anisotropy energy KV to the Zeeman energy μB, while σ is the ratio of anisotropy and thermal energy. Also K/M is a characteristic value for the anisotropy field B_{ani}; half the maximum to be precise. Due to this increased complexity, we restrict the analysis to parameters typical for iron-oxide MNPs (cf. Sec. IV A).

Technically, the ratio of ω_0 to the Larmor frequency, γB, and to the superparamagnetic frequency [61,69], ω_{S} (the rate of thermally driven, zero-field moment reversals) are independent, dimensionless parameters. For the simulations here, $\omega_0 \ll \gamma B$ so ferromagnetic resonance is negligible [70] and in most cases $\omega_0 \gg \omega_{\text{S}}$, i.e., the particles are blocked on the timescale of a single field oscillation. Therefore, we expect neither superparamagnetism nor ferromagnetic resonance to affect the simulated hysteresis response. Then field frequency only enters the relevant dimensionless parameters via the product $\omega_0\zeta_\perp^{\text{r}}$ in β [cf. Eq. (19)]. Hence, like in Fig. 3, varying $\zeta_\perp^{\text{r}}$ gives a different absolute absorption rate than varying ω_0, but is equivalent in terms of intrinsic dynamics like the shape of the hysteresis curve.

We are not aware of any general, analytical solutions, so we use time-step integration to simulate the spheroids rotation as described in Appendix D. In the Supplemental Material [68] we validate the simulation against analytical results on Brownian diffusion [71]. To elucidate the effect particle shape has on energy absorption and dissipation, we compute the time-average of the input power Eq. (16), the viscous losses from rotational drag Eq. (18) and the magnetic losses from Gilbert damping Eq. (17). That is, we infer $\langle P_{\text{mag}}\rangle$ from $\langle P_{\text{hyst}}\rangle$, $\langle P_{\text{rot}}\rangle$ and energy conservation as this is easier to converge numerically than using Eq. (17) directly.

Typically, power transfers are reported per mass of MNPs in the sample. In particular, $\langle P_{\text{hyst}}\rangle$ per mass is known as the specific absorption rate (SAR). Since mass does not enter our model, we give the averaged powers per volume of magnetic material instead.

For a lone particle, the shape affects the viscous friction and the shape anisotropy (cf. Fig. 2). To isolate the effect of friction, we simulate both with and without shape anisotropy.

A. Parameters

In Secs. IV B 1 and IV B 2 we consider five spheroids with aspect ratios of $p = 0.1, 0.5, 1, 2, 10$, but all with the same volume as a 20 nm diameter sphere. Thus, we can imagine a fixed volume of magnetic material moulded into five different shapes, as shown in Fig. 2. For the computations without shape anisotropy Fig. 4, we also simulated the equivalent sphere of the $p = 10$ spheroid, to verify the equivalence discussed in Sec. II E. In Sec. IV C we vary aspect ratio at five fixed field strengths. All other parameters are kept constant.

In the Supplemental Material [68] we justify the uniform magnetization assumption by comparing to literature results [45,48,49], where we use the exchange length for maghemite [72] $L_{\text{ex}} = 46.6$ nm.

$\eta = 1$ mPa s is the viscosity of water at $T = 300$ K. A frequency of $f = 100$ kHz is relevant for hyperthermia applications. The magnetization $M = 400$ kA/m and effective anisotropy $K_0 = 20\,\text{kJ/m}^3$ are representative of maghemite spheres [73], though both higher [74] and lower [75] anisotropy values have been reported and surface effects greatly increase K_0 for smaller particles [73]. Determining the Gilbert damping constant, α, for different materials is an active area of research, so we simply used 0.01 which is between bulk Fe and bulk Ni [76].

It has been shown for a sphere with similar parameters [27] that at zero temperature there is a sharp transition from viscous losses to predominantly magnetic when B is slightly above K/M, i.e., when $\kappa < 1$. In general, at $T = 0$, K/M serves as a lower bound [26,27,77]. Here $K_0/M = 50$ mT, so to study both loss modes, we vary the field from 20 to 100 mT when neglecting shape anisotropy. With shape anisotropy, K increases by about a factor of 3 for the needle shape [see $p = 10$ in Fig. 2(b)], hence we simulate B from 20 to 300 mT instead.

At $B = 20$ mT the dimensionless temperature parameter [see Eq. (20)] is $\epsilon = 0.12$, corresponding to the light-blue region of Fig. 3, so most simulations are in a low-temperature regime. Similarly, $\sigma = 20$ for the sphere [cf. Eq. (22)], in which case superparamagnetism is negligible. In Fig. 6 some of the $p < 1$ spheroids are superparamagnetic, since $K \approx 0$ for $p \approx 0.6$, but this coincides with low SAR so we do not investigate this regime in detail.

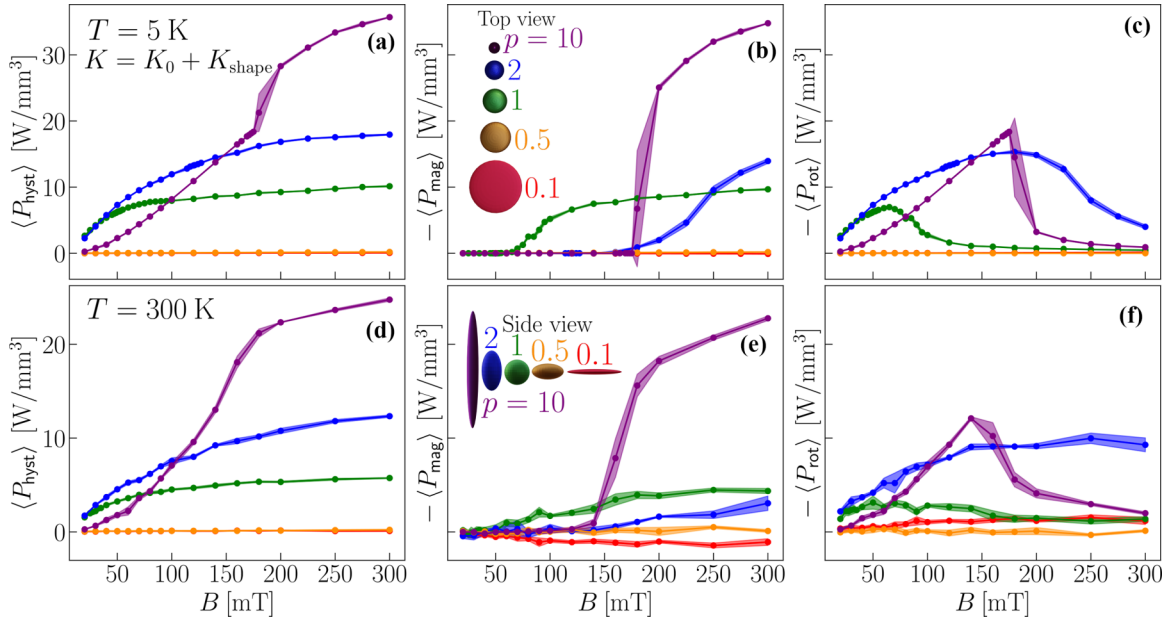

FIG. 5. Same as Fig. 4, except that shape anisotropy is included and each datapoint is the mean of three simulations.

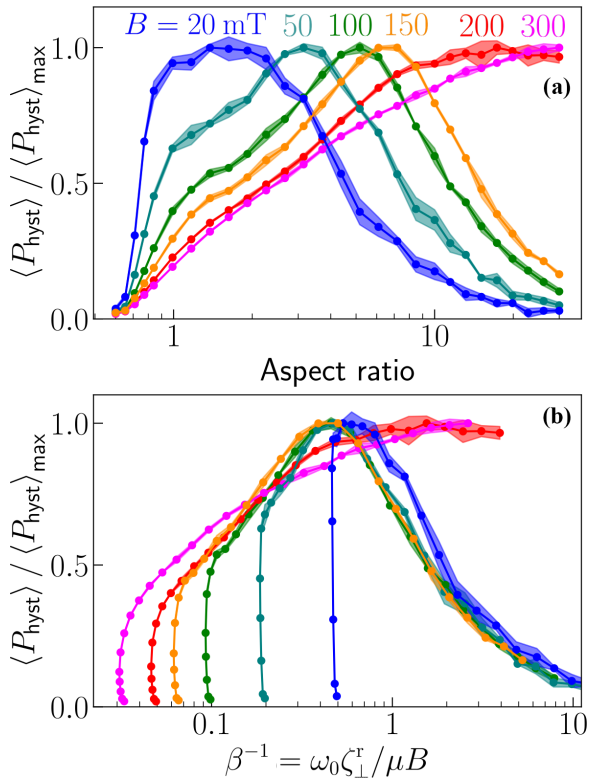

FIG. 6. (a) Absorption power vs aspect ratio at 6 different field amplitudes. $\langle P_{\text{hyst}}\rangle$ is normalized by the highest simulated value at a given field amplitude. (b) Same data as a except shown as function of the dimensionless parameter $\beta^{-1} = \omega_0\zeta_\perp^{\text{r}}/\mu B$ which is a function of aspect ratio via $\zeta_\perp^{\text{r}}$ [cf. Fig. 2(b)]. The nearly vertical lines correspond to aspect ratios $\lesssim 1$, where $\zeta_\perp^{\text{r}}$ is nearly constant, but K varies greatly (cf. Fig. 2).

B. Energy transfer versus field strength

1. Without shape anisotropy

Figure 4 shows the time-average power of the three different energy transfer channels [cf. (15)–(18)]. We neglect shape anisotropy, so only the friction coefficients change [cf. Fig. 2(a)].

For $p = 10$, the results for the equivalent sphere (purple circles) are identical to the spheroid results (purple points) within uncertainty. The equivalent sphere has the same parameters by construction, except higher values of $\zeta_\perp^{\text{t}}$, $\zeta_\parallel^{\text{t}}$ and 10 times as high $\zeta_\parallel^{\text{r}}$. Hence, the equivalence demonstrates how only the transverse, rotational friction coefficient $\zeta_\perp^{\text{r}}$ matters.

$\zeta_\perp^{\text{r}}$ changes little between the shapes with $p = 0.5, 1, 2$, especially the sphere and the $p = 0.5$ flattened sphere, which is why they exhibit similar behavior throughout. For the more extreme aspect ratios, $p = 0.1, 10$ there is a significant increase in drag, especially for the $p = 10$ needle shape.

In Figs. 4(a)–4(c) we see a sharp transition from only viscous losses to predominantly magnetic losses for $p = 0.1, 10$, beginning around $B = K/M = 50$ mT, which is in agreement with the literature [25–27]. For $p = 0.5, 1, 2$ magnetic losses also begin to occur for $B \gtrsim K/M$, however with a gradual transition from viscous to magnetic.

At a temperature of $T = 300$ K, Figs. 4(d)–4(f), the $p = 0.1, 10$ shapes retain a more gradual viscous to magnetic transition, albeit at a reduced switching field of around $B = 35$ mT, while for the other shapes, the rotational losses are equal or greater than magnetic throughout. In the terminology of Ref. [25] there is a clear viscous mode at low temperature, and a clear viscous-magnetic transition at high friction, but otherwise significant thermal mode-mixing occurs.

We note that while increased temperature typically decreases the overall scale of energy transfer, like in the RDA

case, there are counterexamples. In particular, for the needle in the interval $B \approx 30...50$ mT thermal fluctuations increases absorption because the magnetic mode is activated at a lower field strength.

The $p = 0.1$, 10 shapes have $\beta < 1$ for $B < 40$ mT, while the three nearly spherical shapes have $\beta > 1$ throughout, which may explain the qualitatively different slopes in the viscous and mixed-mode regions.

Increased drag generally reduces frictional losses in the simulated cases, but magnetic losses increase, which more than compensates at high field strength. From Fig. 4(d) we see that the needle is the best energy absorber at high B while a nearly spherical shape is optimal at low B, with a transition around $B = 30$ mT. In the small interval $B \approx 35...40$ mT the disk has highest SAR, as the intermediate drag enables high frictional and magnetic losses simultaneously.

In the limiting case of $p \to \infty$, the friction coefficient $\zeta_\perp^{\mathrm{r}}$ also diverges, so that all mechanical motion ceases. This is equivalent to embedding a particle with the same R, M and K values in a solid. Figure 4(d) suggests that this maximizes absorption at very high field strength, i.e., when $B \gg K/M$.

2. With shape anisotropy

In Fig. 5, shape anisotropy is included, so the anisotropy values K correspond to the blue curve in Fig. 2(b).

Here the two flattened shapes, $p = 0.5, 0.1$ have $K < 0$ which means easy-plane, hard-axis anisotropy. Because the moment can rotate in this easy-plane, it can align with the external field without crossing any energy barriers, which is why there is almost zero absorption [see red and orange curves in Figs. 5(a) and 5(d)]. At $T = 5$ K we see from Figs. 5(b) and 5(c) that both magnetic and viscous losses are essentially zero, so there is no mechanical motion in steady-state. Conversely, in Figs. 5(e) and 5(f) we see net energy transfers in both the magnetic and viscous channel at $T = 300$ K; however, this is a consequence of thermal fluctuations. For $p = 0.1$ in particular, it appears $\langle P_{\mathrm{mag}} \rangle$ is consistently positive and $\langle P_{\mathrm{rot}} \rangle$ negative however further simulations at finer timestep (not shown) indicate that this is a numerical artefact.

For the sphere and two elongated shapes $K > 0$, so the $T = 5$ K behavior is qualitatively similar to Fig. 4, i.e., a more or less gradual transition between viscous and magnetic losses beginning at a critical field strength. The difference is that the greater K resulting from shape anisotropy increases the critical field, which is evident in Fig. 5(b). The higher energy barrier also greatly increases the absorption rate when the critical field is reached (note the different scales of the xy axes between Figs. 4 and 5). We note that from the $B \geqslant K/M$ criterion, the lower bounds are 110 mT for $p = 2$ and 168 mT for $p = 10$. With low drag (blue and green curves), the absorption rate increases smoothly, while at high drag (purple curve) there is a sudden increase when switching from viscous to magnetic dissipation.

At room temperature, Figs. 5(d)–5(f), the $p = 2$ spheroid has greater absorption than the sphere throughout, while the $p = 10$ needle is the optimal heater from $B = 100$ mT rather than the 150 mT observed at $T = 5$ K. We conclude that for hysteresis heating, thermal fluctuations favour a higher aspect ratio. This might be because thermal fluctuations generally reduce heating power, as exemplified by the RDA analysis Fig. 3, but the increased anisotropy energy barrier reduces the fluctuations. Indeed, the needle is the one which changes least from 5 to 300 K in terms of the viscous-magnetic transition.

C. Absorption rate versus aspect ratio

Here we study how the absorption rate can be tuned through aspect ratio for a given material, particle volume, and applied field.

From Fig. 6(a), it is seen that the absorption rate approaches zero for the lowest aspect ratios, i.e., when $K \to 0$. Together with Figs. 5(a) and 5(d), this demonstrates that $K > 0$ is necessary for hysteresis. For $B = 20, 50, 100, 150$ mT there is an optimal aspect ratio between 1 and 10 while at $B = 200, 300$ mT the optimum is for even more elongated particles. Since K is nearly constant for $p > 10$ increasing p further only increases friction, so the analysis from Sec. IV B 1 is applicable. Thus, at high field strength we expect the maximum absorption rate to be in the $p \to \infty$ limit, which is equivalent to an immobilized particle aligned with the applied field.

In Fig. 6(b) we show the same data as function of $\beta^{-1} = \omega_0 \zeta_\perp^{\mathrm{r}} / \mu B$, i.e., the same parameter we varied in Fig. 3 except inverted so it increases with increasing p. At intermediate field strengths, $B = 50...150$ mT, the maximal absorption in every case is around $\beta^{-1} \approx 0.5$, i.e., when

$$\zeta_\perp^{\mathrm{r}} = \mu B / 2\omega_0, \tag{23}$$

and the curves coincide at high p. At low p, there is an almost vertical drop in absorption, which is because $\zeta_\perp^{\mathrm{r}}$ changes little from $p = 1$ to 0.6, but the anisotropy vanishes (cf. Fig. 2). For $B = 20$ mT the vanishing of K nearly coincides with the optimal shape and the curve is slightly shifted—probably because greater ϵ means thermal fluctuations play a greater role—but otherwise we see the same trend. Thus, for a broad range of field amplitudes, we find nearly the same optimization criterion as the RDA analysis in Sec. III, i.e., $\beta \sim 2$ to maximize viscous dissipation from rotation. At high fields, the optimum is to maximize p independent of β.

The different behaviors and optimization criteria can be understood in terms of the viscous and magnetic mode. At low K—here for slightly flattened shapes—$B \gg K/M$ so we are in the magnetic regime, however the anisotropy barrier is small implying little hysteresis. Also if σ is small, thermal fluctuations induce superparamagnetic moment reversals, which may also affect energy absorption. Increasing p always increases K until the spheroid either transitions to the viscous mode or reaches the maximum anisotropy, which is (cf. Appendix A)

$$K_{\max} = K_0 + \lim_{p \to \infty} K_{\mathrm{shape}} = K_0 + \tfrac{1}{4}\mu_0 M^2, \tag{24}$$

and in the present case $K_{\max} = 70\,\mathrm{kJ/m^3}$. When $K = K_{\max}$, the critical field for switching mode is around $K_{\max}/M = 175$ mT.

If $B \gg K_{\max}/M$, then the system is in the magnetic mode for all particle shapes and the optimum is the $p \to \infty$ limit where the anisotropy barrier is largest. This is the case at 200 and 300 mT.

If instead $B \lesssim K_{\max}/M$, then the maximal absorption rate will occur in the viscous- or mixed mode. This is the case for the $B \leqslant 150$ mT simulations, so the total absorption is maximized by the $\beta \sim 2$ criterion [Eq. (23)].

V. OPTIMAL SHAPE

There are applications where minimal energy dissipation is desirable, e.g., power electronics [10], but here we focus on how to optimize the system for magnetic hyperthermia treatment and other heating applications. Thus, we want to maximize energy absorption.

We found above that in all cases, increasing B raises the absorption rate. For B around the magnetic-viscous transition, thermal fluctuations may increase absorption by activating the magnetic mode, but in general increasing T lowers the absorption. This makes sense as energy absorption must equal dissipation in steady-state and B drives both mechanical rotation (viscous losses) and moment rotation (magnetic losses). The more the system is driven by random, thermal noise instead, the weaker is the field-particle coupling and consequent energy transfer. Thus, ironically, thermal fluctuations tend to interfere with further heating.

Lowering temperature defeats the point of hysteresis heating, and increasing field amplitude or frequency is not always desirable, as the power cost for producing an oscillating field scales with $\omega_0 B^2$, hence even as heating power increases, heating efficiency may fall. So with temperature and frequency fixed, what is the optimal MNP shape at a given field strength? This is discussed below.

A. Discussion and recommendations

To summarize the results of Secs. IV B and IV C, the MNP transitions from mechanical rotation with mostly frictional energy losses to moment rotation with primarily magnetic losses, as the strength of the applied field increases, in agreement with literature. While the critical field strength—and whether there is a sudden or gradual transition—depends on field frequency, temperature, and the transverse friction coefficient $\zeta_\perp^{\mathrm{r}}$, it is given by $B = K/M$ to a first approximation. Since K is a function of shape, and will typically reach zero for sufficiently flat shapes, there is a critical aspect ratio, p_0, for any given B where

$$K(p_0) = MB. \tag{25}$$

In practice, K can be calculated from Eq. (A3) if the combined magnetocrystalline, strain, and surface anisotropy K_0 is known. Then p_0 can be computed numerically or read off from Fig. 2(b).

Now imagine taking a spherical MNP and stretching or compressing it along one axis to maximize energy absorption. That is, vary the aspect ratio with all other parameters held fixed, including particle volume. If $B > K_{\max}/M$ where $K_{\max}$ is given in Eq. (24) then magnetic losses dominate for all shapes and the $p \to \infty$ limit is optimal. From Fig. 2(b) we note that $p = 10$ is adequate for saturating the shape anisotropy, though increasing p further still increases magnetic losses via drag.

TABLE II. How to maximize SAR through particle geometry. Also main loss channel with the optimized geometry.

Regime	$\frac{K_{\max}}{M} < B$	$B_{\min} < B \lesssim \frac{K_{\max}}{M}$	$B < B_{\min}$
Geometry opt.	Max p, $\zeta_\perp^{\mathrm{r}}$	$\zeta_\perp^{\mathrm{r}} \approx \frac{\mu B}{2\omega_0}$	$p = p_0$
Main loss channel	Magnetic	Viscous	Both

If $B < K_{\max}/M$ then one reaches the viscous-magnetic transition at finite p so frictional losses must be considered. From both the RDA analysis, Sec. III, and the full dynamics, Sec. IV C, we find that viscous, rotational losses are maximal for $\beta \sim 1$. From Fig. 6(b) it is seen that $\beta \approx 2$ works well—at least for the simulated frequency and temperature—which is equivalent to Eq. (23).

If $\beta(p_0) > 2$, then Eq. (23) can be satisfied by increasing p further. Conversely, if $\beta(p_0) < 2$, then there is already too much drag to effectively drive mechanical rotation, so elongating further is detrimental and $p = p_0$ is reasonable for both viscous and magnetic losses. $\beta(p_0) < 2$ holds if $B < B_{\min}$ where $B_{\min}$ is defined by

$$\mu B_{\min} = 2\omega_0 \zeta_\perp^{\mathrm{r}}[p_0(B_{\min})]. \tag{26}$$

One can either solve Eq. (26) numerically or compute $\beta(p_0)$ for each B value of interest.

The optimization criteria are summarized in Table II.

We note that the rotational friction coefficients are proportional to volume [cf. Eqs. (B1) to (B4)], so $\beta = \frac{MB}{\omega_0}\frac{V}{\zeta_\perp^{\mathrm{r}}}$ is volume independent, as is the switching field K/M. Hence, the results in Table II hold regardless of absolute particle size, as long as the uniform magnetization assumption is valid.

Tuning $\zeta_\perp^{\mathrm{r}}$ can be done either by varying solvent viscosity, the particle shape for a given volume or the hydrodynamic volume at fixed magnetic moment, e.g., using a nonmagnetic coating layer [cf. Eq. (B4)]. For a spheroid in a given driving field, one can compute the ideal friction coefficient from Eq. (23) then read off the corresponding aspect ratio from the $p > 0.84$ part of Fig. 2(b).

While we only simulated spheroids, the optimization criteria in Table II should give reasonable estimates for any shape with rotational symmetry around the anisotropy axis. In general, $\zeta_\perp^{\mathrm{r}}$ may be computed numerically [56,57], but for a sphere in particular it holds that [78] $\zeta_{\mathrm{r}} = 8\pi\eta R_{\mathrm{h}}^3$ where R_{h} is hydrodynamic radius. Thus, for a spherical, core-shell particle, viscous dissipation is maximized by

$$\zeta_{\mathrm{r}} \approx \frac{\mu B}{2\omega_0} \to \eta\left(\frac{R_{\mathrm{h}}}{R_{\mathrm{m}}}\right)^3 \approx \frac{MB}{12\omega_0} \qquad \text{(sphere)},$$

where R_{m} is the radius of the magnetic core.

B. Absorption with optimized shape

For the generic iron oxide simulated (cf. Table I), we estimate that the criterion of Eq. (23) maximizes SAR for field amplitudes between $B_{\min} = 20$ mT [cf. Eq. (26)] and $K_{\max}/M = 175$ mT [cf. Eq. (24)], in agreement with Fig. 6.

We also simulated the absorption rate for the optimized aspect ratio p_{opt} which we determine using Table II. In the $B > K_{\max}/M$ regime we used $p_{\mathrm{opt}} = 30$. The result is shown

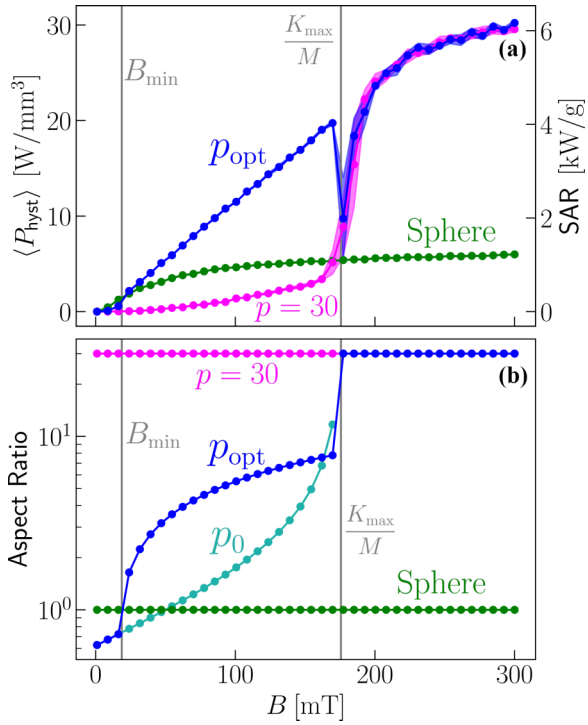

FIG. 7. (a) Absorption rate vs field strength for optimized aspect ratio p_{opt} with comparison to $p = 1$ (sphere) and $p = 30$ (extremely elongated particle). (b) The aspect ratios corresponding to the data in panel (a), in addition to the critical aspect ratio for the magnetic-viscous transition p_0. The density of maghemite $\rho = 4.9$ g/cm^3 was used to convert to SAR (power per MNP mass). Dots are datapoints, lines a guide to the eye and colored regions show uncertainty by the standard deviation of several simulations. Gray lines indicate the estimated upper and lower bounds for the B-interval where optimizing mechanical rotation gives the highest absorption. Note that p_0 diverges at $\frac{K_{\max}}{M}$.

in Fig. 7(a) with a comparison to a sphere ($p = 1$) and needle ($p = 30$). The corresponding aspect ratios are shown in Fig. 7(b) together with p_0, i.e., the aspect ratio where we estimate the viscous-magnetic transition to occur.

We see that for intermediate field strengths, $B \approx 30...175$ mT, using p_{opt} is superior to either extreme, with an improvement of up to more than 200% (e.g., 270% at $B = 170$ mT). When switching to $p = 30$ at $K_{\max}/M = 175$ mT there is a sudden drop in absorption. This is because there is a B range where maximal absorption is achieved in the mixed mode. We do not have simple, general criteria for optimizing this transition regime, hence the steplike change from maximizing viscous losses using Eq. (23) to maximizing magnetic; however, for the present parameters, one could beneficially extend the viscous maximization to higher field strengths.

For low B the sphere actually surpasses the optimized shape [green points are above blue in Fig. 7(a) for $B < B_{\min}$]. The reason is most likely the relatively greater impact of thermal fluctuations at low B where ϵ is higher [cf. Eq. (20)]. In determining p_{opt} we did not account for how anisotropy suppresses thermal noise, nor how said noise impacts the viscous-magnetic transition point.

Interestingly, the greater uncertainty for $B \gtrsim \frac{K_{\max}}{M}$ shows that the magnetic- and mixed modes have greater variation between field cycles than the viscous, so in that sense the magnetic loss channel is noisier than the viscous.

Aside from the drop in the transition regime, $\langle P_{\text{hyst}} \rangle(B)$ is essentially linear, but the energy cost in generating B scales as B^2. Thus, even with shape optimization, the efficiency of the energy transfer from field to particle is lower at high field strength.

In conclusion, the criteria in Table II work well when the optimized shape falls firmly in either the viscous or magnetic mode, and when thermal effects are relatively small, in the sense that $\mu B \gg k_B T$. For $B \sim K_{\max}/M$ where the mixed-mode is optimal, or when thermal fluctuations dominate, further analysis is required. Also, the results are only applicable to dilute suspensions of MNPs with a rotational symmetry axis, so further work is needed for interacting systems and MNPs with more complex anisotropy.

VI. CONCLUSIONS

We used a lone spheroidal MNP with uniaxial anisotropy along the symmetry axis as a model system to study how particle shape affects MNP dynamics and hysteresis heating in liquid suspension under an AC-field. Through numerical simulations at increasing levels of generality, we found that in terms of energy transfer, the only difference between a spheroid and a sphere with uniaxial anisotropy is in the value of input parameters. Specifically, varying the aspect ratio at fixed volume tunes the anisotropy constant and the friction coefficients, of which only the transverse, rotational coefficient is relevant.

When the ratio of Zeeman- to anisotropy energy, MB/K, is small, friction losses dominate (viscous mode), while in the opposite limit magnetic losses dominate (magnetic mode). At zero temperature, it is known that there is a sharp transition at $B \geqslant K/M$ [25–27], but at finite temperature, we find a gradual transition through a mixed-mode regime. For the quasispherical, low friction shapes we observe significant mode-mixing across broad field intervals. Conversely with high friction there is a relatively sharp transition, albeit at a lower critical field due to thermal fluctuations. For blocked particles, far from ferromagnetic resonance, inspecting dimensionless parameters suggests that increasing frequency will produce the same qualitative trends as increasing friction and vice versa. More work is required to elucidate the frequency dependence in the superparamagnetic regime.

In the magnetic mode, elongating the MNP enhances energy transfer, as the increased magnetic hardness increases magnetic losses. That is, until the MNP becomes magnetically hard enough to enter the viscous mode. We determined an optimal value of the friction coefficient where the applied field most efficiently drives the rotational, viscous dissipation. For the typical iron oxide parameters simulated, elongating the MNP to reach this ideal friction gives the highest total energy absorption for all driving fields from about 30 to 175 mT. For higher field amplitudes, all shapes will be in the magnetic mode and extreme elongation maximizes absorption power.

In Sec. V, in particular Table II, we present general criteria to estimate the optimal shape for a given material and applied field, which turn out to be independent of particle volume.

APPENDIX A: SHAPE ANISOTROPY

The shape anisotropy energy, also known as the demagnetization energy or magnetostatic self-energy, for a uniformly magnetized object is [34, Eq. (1)]

$$E_{\text{shape}} = \tfrac{1}{2}\mu_0 M^2 \mathbf{m}^T \mathrm{N}\mathbf{m} = \tfrac{1}{2}\mu_0 M^2 \left(m_1^2 N_1 + m_2^2 N_2 + m_3^2 N_3\right), \quad \text{(A1)}$$

where N is the dimensionless demagnetization tensor, N_1, N_2, N_3 are its eigenvalues and m_1, m_2, m_3 are the moment components in a reference frame where N is diagonal. For a spheroid two of the eigenvalues are identical, say if $m_3 = \mathbf{m}\cdot\mathbf{u}$ then $N_1 = N_2 = N_\perp$ and $N_3 = N_\parallel$. For the trace, it can be shown in general that $\mathrm{Tr}\mathrm{N} = 1$, hence

$$N_\parallel + 2N_\perp = 1 \to N_\perp = \frac{1 - N_\parallel}{2}. \quad \text{(A2)}$$

Inserting in Eq. (A1) and using $m_1^2 + m_2^2 = 1 - m_3^2$ yields

$$E_{\text{shape}} = \frac{\mu_0 M^2}{2}\left[N_\perp + m_3^2 (N_\parallel - N_\perp)\right] = \text{const.} - K_{\text{shape}}(\mathbf{m}\cdot\mathbf{u})^2,$$

where the shape anisotropy constant is

$$K_{\text{shape}} = \frac{\mu_0 M^2}{4}[1 - 3N_\parallel]. \quad \text{(A3)}$$

Thus, for any spheroid, the shape anisotropy is uniaxial and only $N_\parallel$ and the magnetization is needed to compute it.

With some notational changes relative to the source [34, Eqs. (34) and (35)], the demagnetization coefficient along the symmetry axis as a function of aspect ratio p is

$$N_\parallel = \frac{1}{1 - p^2}[1 - G(p)], \quad \text{(A4)}$$

where

$$G(p < 1) = \frac{p}{\sqrt{1 - p^2}} \arctan\left(\frac{\sqrt{1 - p^2}}{p}\right),$$
$$G(p > 1) = \frac{p}{\sqrt{p^2 - 1}} \ln(p + \sqrt{p^2 - 1}). \quad \text{(A5)}$$

When $p = 1$, then $N_\parallel = 1/3$ so $K_{\text{shape}} = 0$. When $p \to \infty$, then $N_\parallel \to \ln(p)/p^2 \to 0$, hence

$$\lim_{p\to\infty} K_{\text{shape}} = \frac{\mu_0 M^2}{4}.$$

APPENDIX B: FRICTION COEFFICIENTS

The drag on a particle moving through liquid at low Reynolds number may be calculated from continuity and the Stokes equation, which is a limiting case of the Navier-Stokes equation. For a spheroid, the exact, closed form solution for the friction coefficients is [35, chap. 3.3]

$$\zeta_\parallel^{\mathrm{t}} = 8\pi\eta\left(\frac{3Vp^2}{4\pi}\right)^{1/3} \frac{(p^2 - 1)}{[2p^2 - 1]G(p) - p^2}, \quad \text{(B1)}$$

$$\zeta_\perp^{\mathrm{t}} = 8\pi\eta\left(\frac{3Vp^2}{4\pi}\right)^{1/3} \frac{2(p^2 - 1)}{[2p^2 - 3]G(p) + p^2}, \quad \text{(B2)}$$

$$\zeta_\parallel^{\mathrm{r}} = 4\eta V \frac{(p^2 - 1)}{[p^2 - G(p)]}, \quad \text{(B3)}$$

$$\zeta_\perp^{\mathrm{r}} = 4\eta V \frac{(p^4 - 1)}{\{[2p^2 - 1]G(p) - p^2\}}. \quad \text{(B4)}$$

This is the same G function as for shape anisotropy Eq. (A5), so it must be characteristic of the spheroid geometry. When $p = 1$, we recover the formulas for a sphere [78],

$$\zeta_\parallel^{\mathrm{t}} = \zeta_\perp^{\mathrm{t}} = 6\pi\eta R, \quad \zeta_\parallel^{\mathrm{r}} = \zeta_\perp^{\mathrm{r}} = 8\pi\eta R^3 \quad (p = 1),$$

where R is radius.

For comparison with the literature, we note that Kim and Karrila [35] use a for the semiaxis of revolution when $p > 1$ (prolate), but c when $p < 1$ (oblate) and express their results in terms of the eccentricity $e = \sqrt{p^2 - 1}/p$. Sergio Aragon [57, Eq. (13)] uses the same G function as this paper but gives the diffusion tensor $\mathrm{D} = k_B T \mathrm{Z}^{-1}$ in terms of $p_{\text{Aragon}} = 1/p$.

APPENDIX C: ANALYSIS OF RDA EQUATION

1. Nondimensionalization

We consider the rigid dipole approximation (RDA), where $\mathbf{m} = \mathbf{u}$, and we neglect the $\gamma^{-1}\dot{\boldsymbol{\mu}}$ term in Eq. (13). Then Eqs. (9) and (13) reduce to

$$\dot{\mathbf{u}} = \boldsymbol{\omega}\times\mathbf{u}, \quad \boldsymbol{\omega} = \mathrm{Z}_{\mathrm{r}}^{-1}[\mu\mathbf{u}\times\mathbf{B} + \boldsymbol{\tau}_{\text{th}}].$$

To apply the inverse friction tensor, we use that

$$\mathrm{Z}_{\mathrm{r}}^{-1}\boldsymbol{\tau}_{\text{th}} = \frac{1}{\zeta_\perp^{\mathrm{r}}}\boldsymbol{\tau}_\perp + \frac{1}{\zeta_\parallel^{\mathrm{r}}}(\boldsymbol{\tau}_{\text{th}}\cdot\mathbf{u})\mathbf{u},$$

where $\boldsymbol{\tau}_\perp$ is the component of $\boldsymbol{\tau}_{\text{th}}$ perpendicular to $\mathbf{u}$, and that $\mathrm{Z}_{\mathrm{r}}^{-1}\mathbf{u}\times\mathbf{B} = \mathbf{u}\times\mathbf{B}/\zeta_\perp^{\mathrm{r}}$. For the motion of the symmetry axis, only the perpendicular angular velocity $\boldsymbol{\omega}_\perp$ matters, so we can write

$$\dot{\mathbf{u}} = \boldsymbol{\omega}_\perp\times\mathbf{u}, \quad \zeta_\perp^{\mathrm{r}}\boldsymbol{\omega}_\perp = \mu\mathbf{u}\times\mathbf{B} + \boldsymbol{\tau}_\perp,$$

which is equivalent to the spherical case, and only one friction coefficient matters.

We now introduce the dimensionless time $\tilde{t} = \omega_0 t$ and angular velocity $\tilde{\boldsymbol{\omega}} = \boldsymbol{\omega}/\omega_0$, and insert Eq. (1) to acquire the final RDA equation

$$\frac{d}{d\tilde{t}}\mathbf{u} = \tilde{\boldsymbol{\omega}}_\perp\times\mathbf{u}, \quad \tilde{\boldsymbol{\omega}}_\perp = \beta\sin(\tilde{t})\mathbf{u}\times\hat{\mathbf{z}} + \tilde{\boldsymbol{\tau}}_\perp, \quad \text{(C1)}$$

where $\tilde{\boldsymbol{\tau}}_\perp = \boldsymbol{\tau}_\perp/\omega_0\zeta_\perp^{\mathrm{r}}$ and β is given in Eq. (19). In a coordinate system with axes along the spheroid semiaxes a, b, c [cf. Fig. 1(b)] and third axis along c, i.e., $\mathbf{e}_3 \parallel \mathbf{u}$, the distribution of $\tilde{\boldsymbol{\tau}}_\perp$ is given by

$$\langle\tilde{\tau}_{\perp,i}(\tilde{t})\tilde{\tau}_{\perp,j}(\tilde{t}')\rangle = \epsilon\beta[\delta_{i1}\delta_{j1} + \delta_{i2}\delta_{j2}]\delta(\tilde{t} - \tilde{t}'), \quad \text{(C2)}$$

for $i, j = 1, 2, 3$, where ϵ is defined in Eq. (20). Thus, the time-evolution of the spheroid is given by just two dimensionless parameters.

2. Optimization of friction coefficient

Under the RDA, particle shape only affects the friction coefficients. Defining the normalized power $\tilde{P}_{\text{hyst}} = \langle P_{\text{hyst}}\rangle/\zeta_\perp^{\mathrm{r}}\omega_0^2$ and recalling the definition of β, Eq. (19), we

find that

$$\frac{d}{d\zeta_\perp^{\mathrm{r}}}\langle P_{\mathrm{hyst}}\rangle = 0 \rightarrow \tilde{P}_{\mathrm{hyst}} + \zeta_\perp^{\mathrm{r}}\frac{d}{d\zeta_\perp^{\mathrm{r}}}\tilde{P}_{\mathrm{hyst}} = 0$$
$$\rightarrow \tilde{P}_{\mathrm{hyst}} = \beta\frac{d}{d\beta}\tilde{P}_{\mathrm{hyst}} \rightarrow \tilde{P}_{\mathrm{hyst}} \sim \beta.$$

That is the stationary points of $\langle P_{\mathrm{hyst}}\rangle$ with respect to aspect ratio are precisely those where $\tilde{P}_{\mathrm{hyst}}$ is linear in β, i.e., the inflection points of $\tilde{P}_{\mathrm{hyst}}$. From Fig. 3 we see this only happens at one β-value for each ϵ, and from the curvature of $\tilde{P}_{\mathrm{hyst}}$ it is seen to be a maximum point for $\langle P_{\mathrm{hyst}}\rangle$.

APPENDIX D: NUMERICAL IMPLEMENTATION

To evaluate the time evolution of the MNP, we time-step integrate the equations of motion, Eqs. (9) and (13). That is, we discretize time into steps of size Δt, which are far shorter than all characteristic timescales in the system. Then torques and effective B fields are essentially constant during a timestep, so we can derive simple, nearly exact formulas for updating the relevant variables from time $t_n = n\Delta t$ to t_{n+1}. Typically, the limiting factor is the Larmor frequency of the precessing magnetic moment, i.e., $\Delta t \ll 1/\gamma B_{\mathrm{eff}}$.

To compute the time-averaged power contributions we write

$$\langle P_{\mathrm{hyst}}\rangle = \Delta E_{\mathrm{hyst}}/t_{\mathrm{int}} \quad \text{where} \quad \Delta E_{\mathrm{hyst}} = \int_{t_0}^{t_0+t_{\mathrm{int}}} P_{\mathrm{hyst}}dt,$$

and equivalently for $P_{\mathrm{rot}}, P_{\mathrm{mag}}$, where t_{int} is integration time and t_0 is an offset to ensure the system has reached steady-state. For maximum time resolution, we update the energy changes, ΔE_{hyst} etc., as part of the timestep procedure. The algorithm goes:

Timestep algorithm
Update $\boldsymbol{\tau}_{\mathrm{th}}, \mathbf{B}_{\mathrm{th}}$
Compute $\boldsymbol{\omega}_n, \boldsymbol{\Omega}_n$
$(\mathbf{m}_n, \mathbf{u}_n) \rightarrow (\mathbf{m}_{n+1/2}, \mathbf{u}_{n+1/2})$
Compute $\boldsymbol{\omega}_{n+1/2}, \boldsymbol{\Omega}_{n+1/2}$
Compute $\dot{E}$ contributions [(16) to (18)]
$\Delta E_{\mathrm{hyst}}^{n+1} = \Delta E_{\mathrm{hyst}}^{n} + \Delta t P_{\mathrm{hyst}}^{n+1/2}$, etc.
$(\mathbf{m}_{n+1/2}, \mathbf{u}_{n+1/2}) \rightarrow (\mathbf{m}_{n+1}, \mathbf{u}_{n+1})$
Repeat from top

To update $\mathbf{m}$ and $\mathbf{u}$ we use the Euler-Rodriguez rotation formula [79]. To compute the thermal B-field we write

$$\mathbf{B}_{\mathrm{th}} = \sqrt{\frac{2k_BT\alpha}{\gamma\mu\Delta t}}\boldsymbol{\xi}_{\mathrm{B}},$$

where $\boldsymbol{\xi}_{\mathrm{B}}$ is a stochastic vector whose components are drawn anew each timestep from independent Gaussian distributions with unit width and zero mean. For the thermal torque,

$$\boldsymbol{\tau}_{\mathrm{th}} = \sqrt{\frac{2k_BT}{\Delta t}}\left[\zeta_\parallel^{\mathrm{r}}(\boldsymbol{\xi}\cdot\mathbf{u})\mathbf{u} + \zeta_\perp^{\mathrm{r}}(\boldsymbol{\xi} - \{\boldsymbol{\xi}\cdot\mathbf{u}\}\mathbf{u})\right],$$

where $\boldsymbol{\xi}$ is defined identically to $\boldsymbol{\xi}_{\mathrm{B}}$.
When updating $\boldsymbol{\omega}, \boldsymbol{\Omega}$ we also update all contributions to $\mathbf{B}_{\mathrm{eff}}$ except $\mathbf{B}_{\mathrm{th}}$ as well as the $\boldsymbol{\mu}\times\mathbf{B}$ and $\dot{\boldsymbol{\mu}}/\gamma$ torques, but not $\boldsymbol{\tau}_{\mathrm{th}}$. This is because, if we do not shift the power evaluations half a timestep relative to updating the thermal fluctuations, the integrated power is subject to artificial, thermal drift. Thermal drift is a general issue when integrating stochastic differential equations [80,81], which is discussed extensively for MNP systems in Ref. [36]. Even with midpoint integration, some thermal drift still occurs because of purely numerical error from the time-discretization, but this primarily occurs in the magnetic losses P_{mag}. So instead of time-averaging P_{mag} directly, we compute the change in total energy $E = \boldsymbol{\mu}\cdot\mathbf{B} - KV(\mathbf{m}\cdot\mathbf{u})^2$ from the configuration $\mathbf{m}(t), \mathbf{u}(t)$, and use energy conservation to get

$$\langle P_{\mathrm{mag}}\rangle = \frac{1}{t_{\mathrm{int}}}[E(t_0+t_{\mathrm{int}}) - E(t_0)] - \langle P_{\mathrm{hyst}}\rangle - \langle P_{\mathrm{visc}}\rangle.$$

We used $\Delta t = 2$ ps for Figs. 4(a)–4(c) and Figs. 5(a)–5(c), $\Delta t = 1$ ps for Figs. 4(d), 4(e) and Figs. 5(d), 5(e) and $\Delta t = 10$ ps for Figs. 6 and 7. In all cases $t_{\mathrm{int}} = 250$ μs and $t_0 = 50$ μs, i.e., of 30 field cycles we set aside 5 to reach steady state.
The simulation procedure for the moment dynamics, including thermal fluctuations, is well-established. To validate our implementation of the mechanical motion, we reproduced known analytical results for the Brownian motion of a freely diffusing ellipsoid [71]. See the Supplemental Material for details [68].
For the RDA computations, we used a reduced version of the same algorithm to simulate the dimensionless equation Eq. (C1). The RDA is multiple orders of magnitude faster to simulate, because neglecting the LLG enables much longer timesteps [24]. Also with a single loss channel (viscous), it is sufficient to compute the total absorbed power $\langle P_{\mathrm{hyst}}\rangle$, which does not suffer from thermal drift.

[1] Q. A. Pankhurst, J. Connolly, S. K. Jones, and J. Dobson, Applications of magnetic nanoparticles in biomedicine, J. Phys. D **36**, R167 (2003).
[2] Q. A. Pankhurst, N. T. K. Thanh, S. K. Jones, and J. Dobson, Progress in applications of magnetic nanoparticles in biomedicine, J. Phys. D **42**, 224001 (2009).
[3] E. A. Périgo, G. Hemery, O. Sandre, D. Ortega, E. Garaio, F. Plazaola, and F. J. Teran, Fundamentals and advances in magnetic hyperthermia, Appl. Phys. Rev. **2**, 041302 (2015).
[4] C. Naud, C. Thébault, M. Carrière, Y. Hou, R. Morel, F. Berger, B. Diény, and H. Joisten, Cancer treatment by magneto-mechanical effect of particles: A review, Nanoscale Adv. **2**, 3632 (2020).
[5] B. Gleich and J. Weizenecker, Tomographic imaging using the nonlinear response of magnetic particles, Nature (London) **435**, 1214 (2005).
[6] N. Panagiotopoulos, R. L. Duschka, M. Ahlborg, G. Bringout, C. Debbeler, M. Graeser, C. Kaethner, K. Lüdtke-Buzug,

H. Medimagh, J. Stelzner, T. M. Buzug, J. Barkhausen, F. M. Vogt, and J. Haegele, Magnetic particle imaging: Current developments and future directions, Int. J. Nanomed. **10**, 3097 (2015).

[7] O. Veiseh, J. W. Gunn, and M. Zhang, Design and fabrication of magnetic nanoparticles for targeted drug delivery and imaging, Adv. Drug Delivery Rev.Targeted Delivery Using Inorganic Nanosystem, **62**, 284 (2010).

[8] M. R. Almind, M. G. Vinum, S. T. Wismann, M. F. Hansen, S. B. Vendelbo, J. S. Engbæk, P. M. Mortensen, I. Chorkendorff, and C. Frandsen, Optimized CoNi nanoparticle composition for Curie-temperature-controlled induction-heated catalysis, ACS Appl. Nano Mater. **4**, 11537 (2021).

[9] S. R. Yassine, Z. Fatfat, G. H. Darwish, and P. Karam, Localized catalysis driven by the induction heating of magnetic nanoparticles, Catal. Sci. Technol. **10**, 3890 (2020).

[10] M. Zambach, M. Varón, M. Knaapila, Z. Ouyang, M. Beleggia, and C. Frandsen, High-susceptibility nanoparticles for microinductor core materials, arXiv:2308.13407.

[11] A. G. Roca, L. Gutiérrez, H. Gavilán, M. E. Fortes Brollo, S. Veintemillas-Verdaguer, and M. D. P. Morales, Design strategies for shape-controlled magnetic iron oxide nanoparticles, Adv. Drug Delivery Rev. **138**, 68 (2019).

[12] J. Li, P. van Nieuwkerk, M. A. Verschuuren, B. Koopmans, and R. Lavrijsen, Substrate conformal imprint fabrication process of synthetic antiferromagnetic nanoplatelets, Appl. Phys. Lett. **121**, 182407 (2022).

[13] R. Mansell, T. Vemulkar, D. C. M. C. Petit, Y. Cheng, J. Murphy, M. S. Lesniak, and R. P. Cowburn, Magnetic particles with perpendicular anisotropy for mechanical cancer cell destruction, Sci. Rep. **7**, 4257 (2017).

[14] M. Goiriena-Goikoetxea, D. Muñoz, I. Orue, M. L. Fernández-Gubieda, J. Bokor, A. Muela, and A. García-Arribas, Disk-shaped magnetic particles for cancer therapy, Appl. Phys. Rev. **7**, 011306 (2020).

[15] M. Ocaña, M. P. Morales, and C. J. Serna, Homogeneous precipitation of uniform α-Fe2O3 particles from iron salts solutions in the presence of urea, J. Colloid Interface Sci. **212**, 317 (1999).

[16] R. Das, J. Alonso, Z. Nemati Porshokouh, V. Kalappattil, D. Torres, M.-H. Phan, E. Garaio, J. Á. García, J. L. Sanchez Llamazares, and H. Srikanth, Tunable high aspect ratio iron oxide nanorods for enhanced hyperthermia, J. Phys. Chem. C **120**, 10086 (2016).

[17] H. Gavilán, K. Simeonidis, E. Myrovali, E. Mazarío, O. Chubykalo-Fesenko, R. Chantrell, Ll. Balcells, M. Angelakeris, M. P. Morales, and D. Serantes, How size, shape and assembly of magnetic nanoparticles give rise to different hyperthermia scenarios, Nanoscale **13**, 15631 (2021).

[18] H. Gavilán, S. Kumar Avugadda, T. Fernández-Cabada, N. Soni, M. Cassani, B. T. Mai, R. Chantrell, and T. Pellegrino, Magnetic nanoparticles and clusters for magnetic hyperthermia: Optimizing their heat performance and developing combinatorial therapies to tackle cancer, Chem. Soc. Rev. **50**, 11614 (2021).

[19] X. Zhu, C. Vo, M. Taylor, and B. R. Smith, Non-spherical micro- and nanoparticles in nanomedicine, Mater. Horizons **6**, 1094 (2019).

[20] T. Potrč, S. Kralj, S. Nemec, P. Kocbek, and M. Erdani Kreft, The shape anisotropy of magnetic nanoparticles: An approach to cell-type selective and enhanced internalization, Nanoscale **15**, 8611 (2023).

[21] M. Cooley, A. Sarode, M. Hoore, D. A. Fedosov, S. Mitragotri, and A. Sen Gupta, Influence of particle size and shape on their margination and wall-adhesion: Implications in drug delivery vehicle design across nano-to-micro scale, Nanoscale **10**, 15350 (2018).

[22] F. L. Durhuus, L. H. Wandall, M. H. Boisen, M. Kure, M. Beleggia, and C. Frandsen, Simulated clustering dynamics of colloidal magnetic nanoparticles, Nanoscale **13**, 1970 (2021).

[23] A. Satoh, R. W. Chantrell, and G. N. Coverdale, Brownian dynamics simulations of ferromagnetic colloidal dispersions in a simple shear flow, J. Colloid Interface Sci. **209**, 44 (1999).

[24] D. V. Berkov, N. L. Gorn, R. Schmitz, and D. Stock, Langevin dynamic simulations of fast remagnetization processes in ferrofluids with internal magnetic degrees of freedom, J. Phys.: Condens. Matter **18**, S2595 (2006).

[25] N. A. Usov and B. Y. Liubimov, Dynamics of magnetic nanoparticle in a viscous liquid: Application to magnetic nanoparticle hyperthermia, J. Appl. Phys. **112**, 023901 (2012).

[26] K. D. Usadel and C. Usadel, Dynamics of magnetic single domain particles embedded in a viscous liquid, J. Appl. Phys. **118**, 234303 (2015).

[27] S. Helbig, C. Abert, P. A. Sánchez, S. S. Kantorovich, and D. Suess, Self-consistent solution of magnetic and friction energy losses of a magnetic nanoparticle, Phys. Rev. B **107**, 054416 (2023).

[28] T. V. Lyutyy, O. M. Hryshko, and A. A. Kovner, Power loss for a periodically driven ferromagnetic nanoparticle in a viscous fluid: The finite anisotropy aspects, J. Magn. Magn. Mater. **446**, 87 (2018).

[29] B. F. Edwards, D. M. Riffe, J.-Y. Ji, and W. A. Booth, Interactions between uniformly magnetized spheres, Am. J. Phys. **85**, 130 (2017).

[30] M. Beleggia, S. Tandon, Y. Zhu, and M. De Graef, On the magnetostatic interactions between nanoparticles of arbitrary shape, J. Magn. Magn. Mater. **278**, 270 (2004).

[31] M. Beleggia and M. De Graef, General magnetostatic shape–shape interactions, J. Magn. Magn. Mater. **285**, L1 (2005).

[32] D. L. Ermak and J. A. McCammon, Brownian dynamics with hydrodynamic interactions, J. Chem. Phys. **69**, 1352 (1978).

[33] S. Bedanta, O. Petracic, and W. Kleemann, Supermagnetism, in *Handbook of Magnetic Materials* (Elsevier, Amsterdam, 2015), Vol. 23, pp. 1–83.

[34] M. Beleggia, M. De Graef, and Y. Millev, Demagnetization factors of the general ellipsoid: An alternative to the Maxwell approach, Philos. Mag. **86**, 2451 (2006).

[35] S. Kim and S. J. Karrila, *Microhydrodynamics: Principles and Selected Applications*, Butterworth-Heinemann Series in Chemical Engineering (Butterworth-Heinemann, Boston, MA, 1991).

[36] F. L. Durhuus, M. Beleggia, and C. Frandsen, Conservation laws for interacting magnetic nanoparticles at finite temperature, Phys. Rev. B **109**, 054421 (2024).

[37] W. Coffey and Y. P. Kalmykov, *The Langevin Equation: With Applications to Stochastic Problems in Physics, Chemistry, and Electrical Engineering*, 4th ed., World Scientific Series in Contemporary Chemical Physics No. 28 (World Scientific, New Jersey, 2017).

[38] E. M. Gubanova, N. A. Usov, and V. A. Oleinikov, Heating ability of elongated magnetic nanoparticles, Beilstein J. Nanotechnol. **12**, 1404 (2021).
[39] N. Usov, Magnetostatic interaction in oriented assembly of elongated nanoparticles, J. Magn. Magn. Mater. **562**, 169804 (2022).
[40] J. H. Sánchez and C. Rinaldi, Rotational Brownian dynamics simulations of non-interacting magnetized ellipsoidal particles in d.c. and a.c. magnetic fields, J. Magn. Magn. Mater. **321**, 2985 (2009).
[41] I. Torres-Díaz and C. Rinaldi, Brownian dynamics simulations of ellipsoidal magnetizable particle suspensions, J. Phys. D **47**, 235003 (2014).
[42] A. Satoh, Brownian dynamics simulations with spin Brownian motion on the negative magneto-rheological effect of a rod-like hematite particle suspension, Mol. Phys. **113**, 656 (2015).
[43] K. Okada and A. Satoh, Regime of aggregate structures and magneto-rheological characteristics of a magnetic rod-like particle suspension: Monte Carlo and Brownian dynamics simulations, J. Magn. Magn. Mater. **437**, 29 (2017).
[44] A. Satoh, Brownian dynamics simulation of a dispersion composed of disk-like hematite particles regarding the orientational distribution and the magneto-rheological properties, Colloids Surf., A **483**, 341 (2015).
[45] W. F. Brown, The fundamental theorem of fine-ferromagnetic-particle theory, J. Appl. Phys. **39**, 993 (1968).
[46] W. F. Brown, The fundamental theorem of the theory of fine ferromagnetic particles*, Ann. N.Y. Acad. Sci. **147**, 463 (1969).
[47] A. Aharoni, Elongated single-domain ferromagnetic particles, J. Appl. Phys. **63**, 5879 (1988).
[48] N. Usov and O. Serebryakova, Nonuniform micromagnetic states in spheroidal magnetite nanoparticles, J. Magn. Magn. Mater. **588**, 171345 (2023).
[49] A. Aharoni, Single-domain ferromagnetic cylinder, IEEE Trans. Magn. **25**, 3470 (1989).
[50] H. Hoffmann and F. Steinbauer, Single domain and vortex state in ferromagnetic circular nanodots, J. Appl. Phys. **92**, 5463 (2002).
[51] E. M. Purcell, Life at low Reynolds number, Am. J. Phys. **45**, 3 (1977).
[52] J. Happel and H. Brenner, *Low Reynolds Number Hydrodynamics*, edited by R. J. Moreau, Mechanics of Fluids and Transport Processes, Vol. 1 (Springer Netherlands, Dordrecht, 1981).
[53] H. Brenner, Coupling between the translational and rotational Brownian motions of rigid particles of arbitrary shape, J. Colloid Interface Sci. **23**, 407 (1967).
[54] B. Cichocki and K. Hinsen, Stokes drag on conglomerates of spheres, Phys. Fluids **7**, 285 (1995).
[55] B. Carrasco and J. García de la Torre, Hydrodynamic properties of rigid particles: Comparison of different modeling and computational procedures, Biophys. J. **76**, 3044 (1999).
[56] J. García de la Torre, G. del Rio Echenique, and A. Ortega, Improved calculation of rotational diffusion and intrinsic viscosity of bead models for macromolecules and nanoparticles, J. Phys. Chem. B **111**, 955 (2007).
[57] S. Aragon, A precise boundary element method for macromolecular transport properties, J. Comput. Chem. **25**, 1191 (2004).
[58] R. Kubo, The fluctuation-dissipation theorem, Rep. Prog. Phys. **29**, 255 (1966).
[59] T. Gilbert, A phenomenological theory of damping in ferromagnetic materials, IEEE Trans. Magn. **40**, 3443 (2004).
[60] S. Streib, N. Vidal-Silva, K. Shen, and G. E. W. Bauer, Magnon-phonon interactions in magnetic insulators, Phys. Rev. B **99**, 184442 (2019).
[61] W. F. Brown, Thermal fluctuations of a single-domain particle, Phys. Rev. **130**, 1677 (1963).
[62] S. J. Barnett, Magnetization by rotation, Science **42**, 163 (1915).
[63] J. Leliaert, J. Ortega-Julia, and D. Ortega, Individual particle heating of interacting magnetic nanoparticles at nonzero temperature, Nanoscale **13**, 14734 (2021).
[64] J. Ortega-Julia, D. Ortega, and J. Leliaert, Estimating the heating of complex nanoparticle aggregates for magnetic hyperthermia, Nanoscale **15**, 10342 (2023).
[65] S. Chikazumi, S. Chikazumi, and C. D. Graham, *Physics of Ferromagnetism* (Oxford University Press, Oxford, UK, 1997).
[66] W. Coffey and Yu.P. Kalmykov, Inertial effects in the complex magnetic susceptibility of a ferrofluid in the presence of a dc bias field, J. Magn. Magn. Mater. **164**, 133 (1996).
[67] K. D. Usadel, Dynamics of magnetic nanoparticles in a viscous fluid driven by rotating magnetic fields, Phys. Rev. B **95**, 104430 (2017).
[68] See Supplemental Material at http://link.aps.org/supplemental/10.1103/PhysRevB.110.144425 for analytical results on the zero temperature limit of the RDA, justification of the uniform magnetization assumption for the simulated particles by comparison to analytical results in the literature and also validation of the general model by comparing simulations to exact results on the statistics of freely diffusing ellipsoids.
[69] W. T. Coffey and Y. P. Kalmykov, Thermal fluctuations of magnetic nanoparticles: Fifty years after Brown, J. Appl. Phys. **112**, 121301 (2012).
[70] D. Slay, D. Cao, E. C. Ferré, and M. Charilaou, Ferromagnetic resonance of superparamagnetic nanoparticles: The effect of dipole–dipole interactions, J. Appl. Phys. **130**, 113902 (2021).
[71] B. Ten Hagen, S. Van Teeffelen, and H. Löwen, Brownian motion of a self-propelled particle, J. Phys.: Condens. Matter **23**, 194119 (2011).
[72] W. Wu, X. H. Xiao, S. F. Zhang, T. C. Peng, J. Zhou, F. Ren, and C. Z. Jiang, Synthesis and magnetic properties of maghemite (γ-Fe2O3) short-nanotubes, Nanoscale Res. Lett. **5**, 1474 (2010).
[73] K. L. Pisane, S. Singh, and M. S. Seehra, Unusual enhancement of effective magnetic anisotropy with decreasing particle size in maghemite nanoparticles, Appl. Phys. Lett. **110**, 222409 (2017).
[74] L. A. Mercante, W. W. M. Melo, M. Granada, H. E. Troiani, W. A. A. Macedo, J. D. Ardison, M. G. F. Vaz, and M. A. Novak, Magnetic properties of nanoscale crystalline maghemite obtained by a new synthetic route, J. Magn. Magn. Mater. **324**, 3029 (2012).
[75] A. Figueroa, J. Bartolomé, L. García, F. Bartolomé, A. Arauzo, A. Millán, and F. Palacio, Magnetic anisotropy of maghemite nanoparticles probed by RF transverse susceptibility, Phys. Procedia **75**, 1050 (2015).

[76] S. M. Bhagat and P. Lubitz, Temperature variation of ferromagnetic relaxation in the 3D transition metals, Phys. Rev. B **10**, 179 (1974).

[77] A. Coene and J. Leliaert, Simultaneous coercivity and size determination of magnetic nanoparticles, Sensors **20**, 3882 (2020).

[78] S. I. Rubinow and J. B. Keller, The transverse force on a spinning sphere moving in a viscous fluid, J. Fluid Mech. **11**, 447 (1961).

[79] H. Cheng and K. C. Gupta, An historical note on finite rotations, J. Appl. Mech. **56**, 139 (1989).

[80] S. Särkkä and A. Solin, *Applied Stochastic Differential Equations*, 1st ed. (Cambridge University Press, Cambridge, UK, 2019).

[81] C. W. Gardiner, *Handbook of Stochastic Methods: For Physics, Chemistry and the Natural Sciences*, study ed., 2nd ed., 6th print ed., Springer Series in Synergetics No. 13 (Springer, Berlin, 2002).